

**In solution adsorption characterization technique
based on the response to an external magnetic field
of porous paramagnetic materials: application on
supramolecular metal-adenine frameworks
containing heterometallic heptameric clusters**

Jon Pascual-Colino,^a Rubén Pérez-Aguirre,^{a,b} Garikoitz Beobide,^{a,c} Oscar Castillo,^{a,c,}*

Imanol de Pedro,^b Antonio Luque,^{a,c} Sandra Mena-Gutiérrez,^a Sonia Pérez-Yáñez^{c,d}

^aDepartamento de Química Orgánica e Inorgánica, Facultad de Ciencia y Tecnología,
Universidad del País Vasco/Euskal Herriko Unibertsitatea, UPV/EHU, Apartado 644,
E-48080 Bilbao, Spain.

^bCITIMAC, Facultad de Ciencias, Universidad de Cantabria, E-39005 Santander, Spain.

^cBCMaterials, Basque Center for Materials, Applications and Nanostructures, UPV/EHU
Science Park, E-48940 Leioa, Spain.

^dDepartamento de Química Orgánica e Inorgánica, Facultad de Farmacia, Universidad
del País Vasco/Euskal Herriko Unibertsitatea, UPV/EHU, E-01006 Vitoria-Gasteiz,
Spain.

INDEX

S1. Infrared spectroscopy	3
S2. Thermal analysis	7
S3. Crystallographic analysis	10
S4. Structural data	13
S5. Computational studies of the pore size distribution	16
S6. Structural flexibility of Cu ₆ Cu upon dehydration/hydration cycles	17
S7. SEM micrographs of compound Cu ₆ Cu	18
S8. N ₂ adsorption isotherms at 77 K for compound Cu ₆ Cu.....	19
S9. Magnetic orbital countercomplementarity	20
S10. Electromagnet characterization and sustentation experiment values	21
S11. Sorption data quantification by ¹ H-NMR.....	23
S12. Elemental analysis of Cu ₆ Cu before and after the sorption experiments.....	28
S13. PXRD studies of Cu ₆ Cu after the sorption experiments.....	29
S14. FTIR studies of Cu ₆ Cu after the sorption experiments.....	30
S15. Comparison between the voids and adsorbate volume and shape.....	31

S1. Infrared spectroscopy

Infrared spectroscopy has been able to determine efficiently the presence of the bands corresponding to the adenine ligand and sulfate counterion. The infrared spectra of the compounds are presented in Figure S1 and S2. Table S1 shows the wave number, the relative intensity and the assignment of the observed bands.

In all cases, the infrared spectra show a wide band around 3400 cm^{-1} characteristic of the O–H stretching of the bridging hydroxides, coordination water molecules and crystallization water molecules. The largeness of the latter band, allows fairly identifying the N–H stretching of the amine group of the adenine as a fine shoulder at ca. 3200 cm^{-1} , but it masks the signals corresponding to the $\text{C}_{\text{ar}}\text{--H}$ stretching expected around 3100 cm^{-1} . Over 1600 cm^{-1} , appears one of the most intense bands of the spectra which is mainly attributable to C=C stretching vibration and deformation vibration of NH_2 group of the adenine. Another representative band of this series of heterometallic compounds appears near of 1108 cm^{-1} which corresponds to S=O vibration of the sulfate counterion.

Table S1.- Infrared spectra bands (cm⁻¹) of the neutral adenine ligand and the herein reported compounds^[a]

Adenine	Cu ₆ Zn	Cu ₆ Cu	Cu ₆ Ni	Cu ₆ Co	Cu ₆ Cr	Assignment ^[b]
–	3400vs	3435vs	3335vs	3335vs	3390vs	v (O–H)
3305s	3200sh	–	3200sh	3200sh	3200sh	v _{as} (NH ₂)
3125s	over	over	over	Over	over	v (C8–H + C2–H)
	1640vs	1640vs	1640vs	1640vs	1640vs	
1605vs	1610vs	1605vs	1600vs	1600vs	1605vs	v (C=N) + v (C=C) + δ (NH ₂)
1560s	1550s	1545s	1545s	1545s	1550s	v (C4–C5 + N3–C4– C5)
1470m	1465m	1465m	1465m	1465m	1465m	δ _{ring} (C2–H + C8–N9) + v (C8–H)
1420s	1400m	1395m	1395m	1400m	1400m	δ _{ring} (N1–C6–H6)
1310s	1305m	1306m	1305m	1305m	1305m	v (N9–C8 + N3–C2) + δ (C–H)
1230s	1195m	1200m	1200m	1200m	1195m	δ _{ip} (CCH)
1265s	1150m	1150m	1150m	1150m	1150m	δ (C8–H) + v (N7–C8)
1110m	1110m	1110m	1110m	1110m	1110m	v _{as} (S–O)
1025w	1030w	1030w	1030w	1030w	1035w	γ (NH ₂)
940w	935w	935w	935w	935w	935w	v (N1–C6) + τ (NH ₂)

^[a]vs = very strong, s = strong, m = medium, w = weak, sh = shoulder, over = overlapping. ^[b]v = tension vibrations, δ = deformation vibrations, γ = rocking, τ = torsion, s = symmetric, as = antisymmetric, ip = in plane.

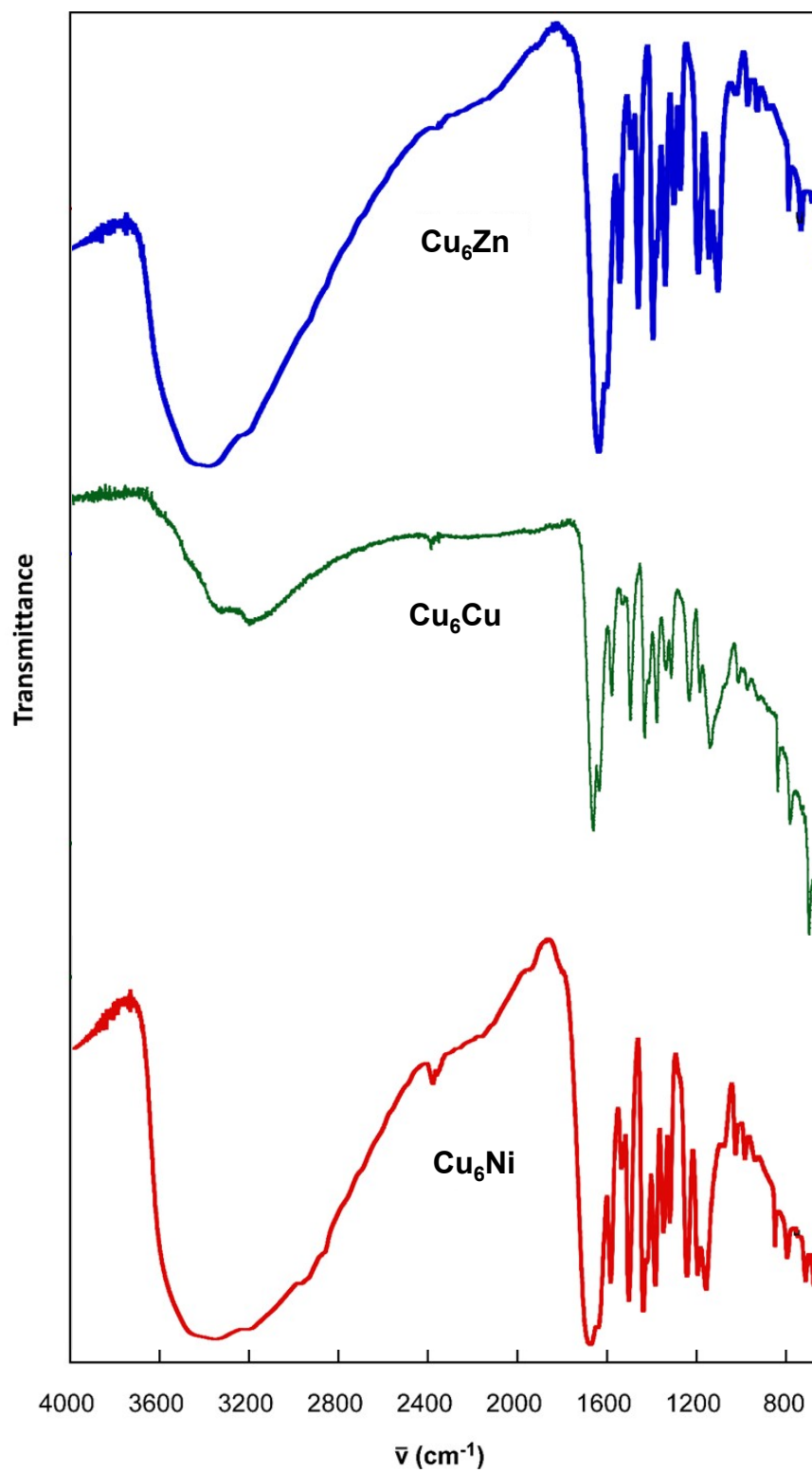


Figure S1.- Infrared spectra of compounds Cu_6Zn (blue), Cu_6Cu (green) and Cu_6Ni (red).

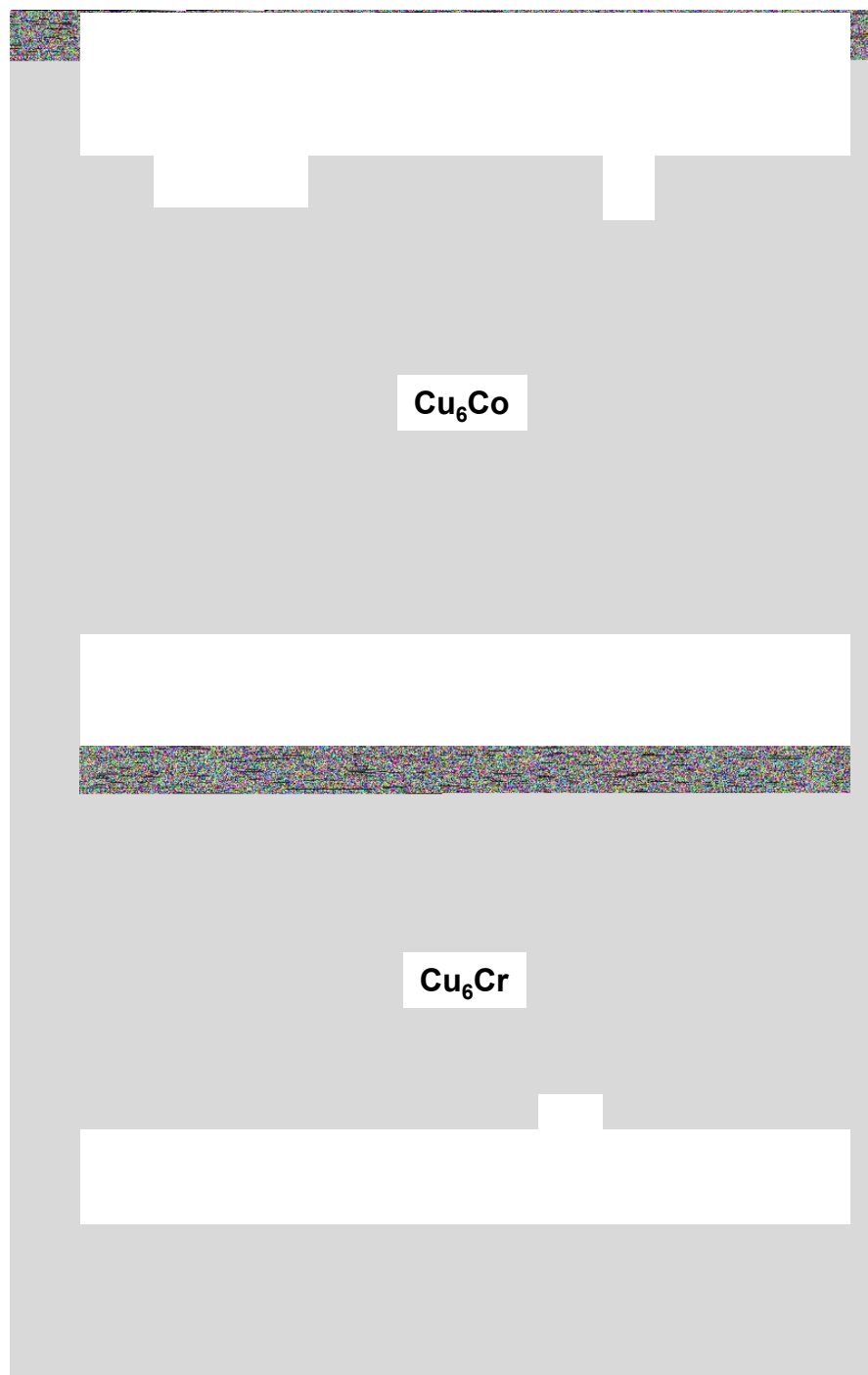


Figure S2.- Infrared spectra of compounds Cu_6Co (green) and Cu_6Cr (red).

S2. Thermal analysis

Thermogravimetric and thermal differential analysis of these compounds are plotted in Figure S3, while the decomposition processes in each degradation stage are gathered in Table S2. All measurements were performed under a synthetic air atmosphere (79 % N₂, 21 % O₂).

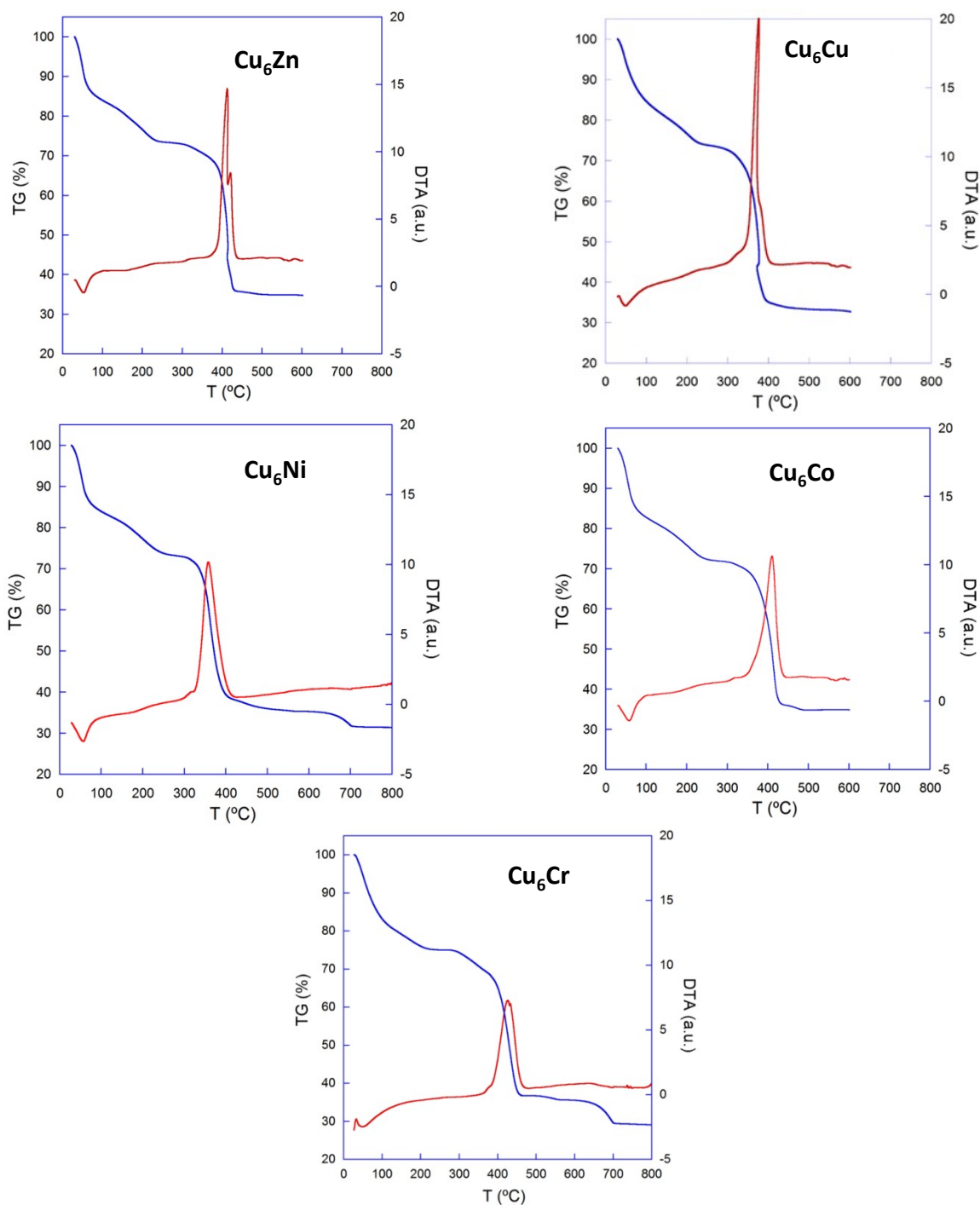


Figure S3.- Thermogravimetric measurements performed on bulk samples.

Table S2.- Thermoanalytic data of the compounds^[a]

Step	T _i	T _f	T _{peak}	ΔH	Δm(%)	ΣΔm(%)	ΣΔm(%) _{theo.} ^[b]
Cu₆Cr							
1	30	95	50	Endo	16.3	16.3	16.3 (-17H ₂ O)
2	95	230	–	–	10.3	26.6	26.6 (-9H ₂ O)
3	300	475	425	Exo	37.9	64.5	64.5 (Cu ₆ CrO ₆ (SO ₄) _{1.5})
4	475	800			6.3	70.8	70.8 (6CuO + 0.5Cr ₂ O ₃)
Cu₆Cu							
1	30		85		16.2	15.9	17.6 (-16H ₂ O)
2	85		135		5.7	21.9	24.4 (-6H ₂ O)
3	135		200		5.3	27.2	27.2 (SO ₄)
4	200		335		5.3	32.5	32.5 (-6NH ₂)
5	335		600		42.1	69.3	69.3 (6CuO)
Cu₆Co							
1	30	65	60	Endo	14.0	14.0	14.0 (-14H ₂ O)
2	65	265	–	–	9.0	23.0	23.0 (-9H ₂ O)
3	290	470	410	Exo	41.8	64.8	64.9 (Cu ₆ CoO ₆ (SO ₄))
Cu₆Ni							
1	30	85	60	Endo	13.5	13.5	13.7 (-14H ₂ O)
2	85	260	–	–	6.9	20.4	20.6 (-7 H ₂ O)
3	290	515	355	Exo	42.7	64.1	64.2 (Cu ₆ NiO ₆ (SO ₄))
4	515	800			4.5	68.6	68.6 (6CuO+NiO)
Cu₆Zn							
1	30	85	55	Endo	15.0	15.0	15.6 (-16 H ₂ O)
2	85	250	–	–	9.3	24.3	23.7 (- 9H ₂ O)
3	290	465	415	Exo	41.2	65.5	66.0 (Cu ₆ ZnO ₆ (SO ₄))

^[a] T_i = initial temperature; T_f = final temperature; T_{peak} = peak temperature ATD; Δm(%) = loss mass percentage in each step; ΔH = type of process according to ATD; ΣΔm(%) = total loss mass after each step; ΣΔm(%)_{theo.} = total loss mass theoretically calculated. ^[b] Eliminated water molecules and final residue per compound formula.

All the compounds display a similar decomposition process. First, the loss of the crystallization water molecules occurs, in an endothermic process, from room temperature to a value below 100 °C. Subsequently, partially overlapped with the previous mass loss process, it takes place the loss of nine water molecules, corresponding to the six bridging waters and to the three water

molecules formed upon the condensation process of the six hydroxide bridges. Despite water desorption and hydroxide condensation reactions are endothermic and exothermic processes, respectively, no clear peak in the DTA curve is observed.

Thereafter, the decomposition of the organic part occurs through a strong exothermic process, generating a residue consisting on copper(II) oxide and the central metal sulfate according to PXRD analysis. In compounds **Cu₆Zn**, **Cu₆Cu** and **Cu₆Co**, where the final analysis temperature was set at 600 °C, no further mass changes are observed. On the other hand, in compounds **Cu₆Cr** and **Cu₆Ni**, the analysis was performed until 800 °C, in such a way that the decomposition process of the metal sulfate to the corresponding oxide is observed. This process allows corroborating the sulphur content set from the crystallographic analysis, as the mass loss is ascribed to the release of SO₃.

S3. Crystallographic analysis

The crystallographic data, the refinement conditions, and parameters of the resolution of compounds have been gathered in Table S3. All non-hydrogen atoms were refined anisotropically, except those corresponding to disordered entities. The hydrogen atoms belonging to adeninato ligands have been geometrically fixed and refined according to a riding model with an isotropic thermal parameter linked to the atom to which they are attached (120 %). The hydrogen atoms of the coordination crystallisation water molecules and hydroxide groups have been located in the difference Fourier map or using the routine CALC-OH implemented in WinGX interface. The refinement of the latter hydrogen atoms has been performed with an isotropic thermal parameter of 150 % respect to their parent atom. Regarding the crystallization water molecules, not all of them could be located due their high disorder and therefore, their contribution was removed using the SQUEEZE procedure as implemented in the PLATON software. Accordingly, the hydrogen atoms of the located crystallization water molecules were not included due to high disorder present within the voids.

Compound **Cu₆Zn** was refined as a two component twin with a batch scale factor (BASF) parameter of 0.420. During the structural resolution of the heptameric entities of **Cu₆Co**, the initial resolution showed anomalous elongated ellipsoids for a series of atoms attributed to the adeninato ligands. These large values of the thermal movements were related to a disorder implying two coplanar puric bases with inverted dispositions regarding the bridging mode ($\mu\text{-}\kappa\text{N}3:\kappa\text{N}9 / \mu\text{-}\kappa\text{N}9:\kappa\text{N}3$). This disorder has been modelled by refining the occupation of each part (A and B) and ensuring they sum up a total occupation factor of one. Furthermore, in compound **Cu₆Co** the use of several restraints (DFIX and FLAT) were required in order to retain the expected geometry of the adeninato ligands during the data refinement process.

In compounds **Cu₆Cu** and **Cu₆Co**, there are two symmetry related sulfate anions per heptamer. Thus, the occupation factors of the atoms comprising the sulfate have been fixed to the stoichiometrically required, i.e., 0.5 and 0.5 respectively. In compound **Cu₆Zn**, there are also two sulfate anions per heptamer, but each sulfate appears grouped together with two crystallization water molecules (O2w, O4w) in such a way that this ensemble is disordered in six positions related by a $\bar{6}$ rotoinversion axis. Accordingly, the occupation factor of the atoms comprising the ensemble has been set to 1/6.

Although the lack of suitable single crystals has prevented the structural resolution of **Cu₆Ni** compound, a profile fitting of its PXRD pattern has yielded similar cell parameters (Table S4 and Figure S4) to those of compound **Cu₆Cu**. Therefore, they can be considered isostructural compounds.

Table S3.- Crystallographic data and refinement details of compounds **Cu₆Zn**, **Cu₆Cu** and **Cu₆Co**

	Cu₆Zn	Cu₆Cu	Cu₆Co
Formula	C ₃₀ H ₁₀₆ Cu ₆ N ₃₀ O ₄₈ SZn	C ₃₀ H ₇₈ Cu ₇ N ₃₀ O ₃₄ S	C ₃₀ H ₁₁₂ CoCu ₆ N ₃₀ O ₅₁ S
M (g·mol ⁻¹)	2134.11	1880.06	2181.72
Cryst. syst.	Trigonal	Orthorhombic	Trigonal
Space group	<i>R</i> ³ <i>c</i>	<i>Cccm</i>	<i>R</i> ³ <i>c</i>
<i>a</i> (Å)	19.108(1)	10.5080(3)	19.058(3)
<i>b</i> (Å)	19.108(1)	24.8920(8)	19.058(3)
<i>c</i> (Å)	43.046(3)	27.0312(9)	43.157(9)
V (Å ³)	13610.9(17)	7070.4(4)	13575(5)
Z	6	4	6
ρ _{calcd} (g·cm ⁻³)	1.375	1.766	1.601
Colour	Light blue	Light blue	Blue
F(000)	5832	3836	6762
λ (Å)	0.71073	0.71073	1.54184
μ (cm ⁻¹)	1.742	2.200	4.095
Meas./indep. refl.	29410/3284	27320/3846	27448/2581
Obs. refl. [I>2σ(I)]	1552	2252	571
R1,wR2 [I>2σ(I)] ^[a,b]	0.0876/0.2612	0.1134/0.3207	0.1058/0.2648
R1,wR2 (all)	0.1643/0.3055	0.1550/0.3398	0.2402/0.3189
Gof (S) ^[c]	1.024	1.073	0.785
Parameters	155	192	118
Max./min. Δρ (e·Å ⁻³)	1.591/-0.593	2.355/-0.940	0.813/-0.459

^[a] $R1 = \sum ||F_o| - |F_c|| / \sum |F_o|$. ^[b] $wR2 = [\sum w(F_o^2 - F_c^2)^2 / \sum wF_o^2]^{1/2}$; $w = 1/[\sigma^2(F_o^2) + (aP)^2 + bP]$, where $P = (\max(F_o^2, 0) + 2F_c^2)/3$. $a = 0.1629$ (**Cu₆Zn**), $a = 0.1854$ and $b = 99.9101$ (**Cu₆Cu**), $a = 0.1345$ (**Cu₆Co**). ^[c] $S = [\sum w(F_o^2 - F_c^2)^2 / (N_{obs} - N_{param})]^{1/2}$.

Table S4.- Crystal data and refinement details obtained from PXRD data for compound **Cu₆Ni**.

Cu₆Ni			
Formula	C ₃₀ H ₆₆ Cu ₆ N ₃₀ NiO ₂₈ S	Z	4
M (g·mol⁻¹)	1767.07	Colour	Blue
Cryst. Syst.	Orthorhombic	ρ_{calcd} (g·cm⁻³)	1.345
Space group	<i>Cccm</i>	2θ range (°)	5.01 – 69.98
a (Å)	10.559(1)	Δ2θ step (°)	0.026
b (Å)	25.048(2)	Time per step (s)	2
c (Å)	27.301(4)	χ²	3.66
α (°)	90	R_f^a	1.73
β (°)	90	R_b^b	1.44
γ (°)	90	R_p^c	20.4
V (Å³)	7220.6(1)	R_{wp}^d	20.2

^a $R_f = \sum | (I_{obs})^{1/2} - (I_{calc})^{1/2} | / \sum (I_{obs})^{1/2}$, ^b $R_b = \sum | I_{obs} - I_{calc} | / \sum I_{obs}$, ^c $R_p = \sum | y_{i_{obs}} - y_{i_{calc}} | / \sum y_{i_{obs}}$, ^d $R_{wp} = [\sum \omega_i | y_{i_{obs}} - y_{i_{calc}} |^2 / \sum \omega_i (y_{i_{obs}})^2]^{1/2}$.

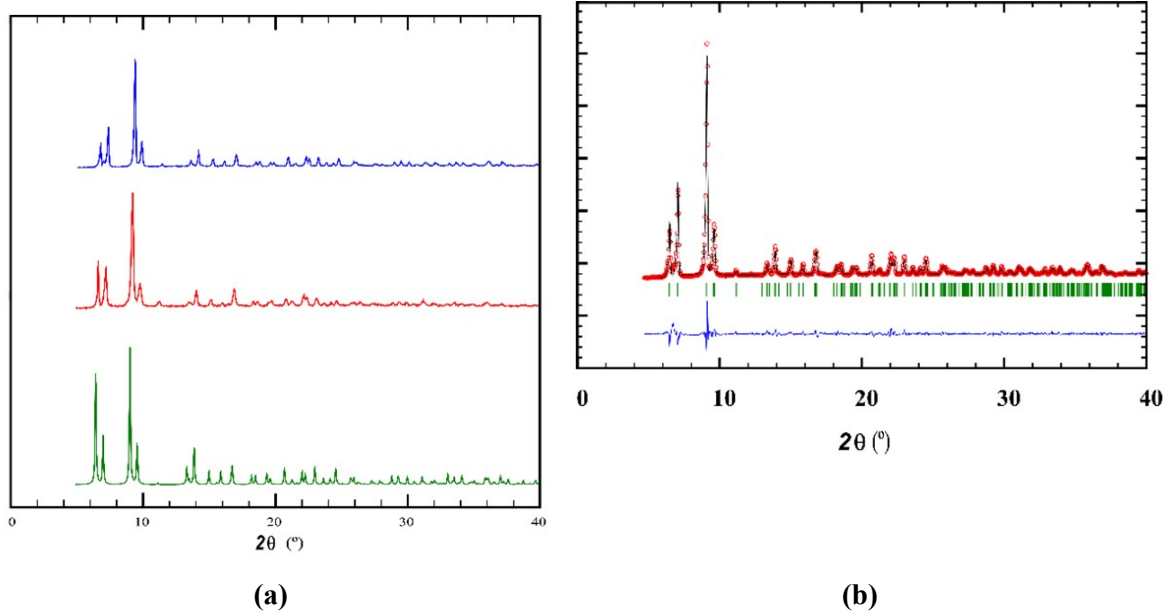


Figure S4.- (a) Comparison of the experimental PXRD of **Cu₆Ni** (blue) with the simulated (green) and experimental (red) ones of **Cu₆Cu**. (b) Profile fitting of the PXRD pattern of **Cu₆Ni**.

S4. Structural data

Table S5.- Coordination bond distances (Å) compounds **Cu₆Zn**, **Cu₆Cu** and **Cu₆Co**.¹

Cu₆Zn					
Zn1–O1	2.075(5)	Zn1–O1 ^c	2.075(1)		
Zn1–O1 ^a	2.075(5)	Zn1–O1 ^d	2.075(1)		
Zn1–O1 ^b	2.075(5)	Zn1–O1 ^e	2.075(1)		
Cu2–N3 ^a	2.009(7)	Cu2–O1 ^c	1.974(4)		
Cu2–N9	1.963(7)	Cu2–O1w ^a	2.440(6)		
Cu2–O1	1.974(5)	Zn1···Cu2	3.114(9)		
Cu₆Cu					
Cu1–N13	1.969(1)	Cu2–O1 ^b	1.975(7)	Cu3–O1w	2.286(8)
Cu1–N13 ^a	1.969(1)	Cu2–O1 ^c	1.975(7)	Cu1···Cu2	3.006(2)
Cu1–O1	1.983(7)	Cu2–O2	2.310(9)	Cu1···Cu3	3.100(2)
Cu1–O1 ^a	1.983(7)	Cu2–O2 ^b	2.310(9)	Cu2···Cu3	3.165(1)
Cu1–O1w	2.497(8)	Cu3–O1	2.001(7)	Cu3···Cu3 ^c	3.141(2)
Cu1–O1w ^a	2.497(8)	Cu3–O2	1.948(5)		
Cu2–O1	1.975(7)	Cu3–N19	1.984(9)		
Cu2–O1 ^a	1.975(7)	Cu3–N23	1.975(1)		
Cu₆Co					
Co1–O1	2.093(1)	Cu1–N13B ^e	1.897(1)		
Co1–O1 ^a	2.093(1)	Cu1–N19A ^e	1.896(1)		
Co1–O1 ^b	2.093(1)	Cu1–N19B	1.900(1)		
Co1–O1 ^c	2.093(1)	Cu1–O1	1.977(1)		
Co1–O1 ^d	2.093(1)	Cu1–O1 ^e	1.946(1)		
Co1–O1 ^e	2.093(1)	Co1···Cu2	3.103(2)		
Cu1–N13A	1.896(12)				

¹ Symmetry-codes. **Cu₆Zn**: (a) $y, -x + y + 1, -z + 1$; (b) $-y + 2, x - y + 1, z$; (c) $x - y, x, -z + 1$; (d) $-x + 2, -y + 2, -z + 1$; (e) $-x + y + 1, -x + 2, z$. **Cu₆Cu**: (a) $-x, -y, z$; (b) $-x, -y, -z$; (c) $x, y, -z$. **Cu₆Co**: (a) $-x, -y, -z + 1$; (b) $x - y, x, -z + 1$; (c) $-x + y, -x, z + 1$; (d) $-y, x - y, z + 1$; (e) $y, -x + y, -z + 1$.

Table S6.- Hydrogen-bonding parameters (Å, °) and π - π in compound **Cu₆Zn**.¹

Cu₆Zn					
D-H...A^[a]	H...A	D...A	D-H...A		
O1-H1...O1S ^a	1.82	2.80(3)	172		
O1-H1...O4S ^b	2.02	2.90(2)	148		
O1-H1...O2w	1.91	2.82(2)	154		
N6-H6A2...O1S	2.08	2.92(4)	169		
N6-H6A2...O2w ^c	2.43	3.24(3)	157		
N6-H6A2...O4S ^d	2.07	2.87(3)	154		
π - π interactions ^[b]					
Ring...Ring	α	DC	β	DZ	DXY
p1...p1 ^[c]	0	4.02	31.2	3.437(4)	2.085

¹Symmetry-codes: (a) $-x + y + 2/3, y + 1/3, z - 1/6$; (b) $-y + 5/3, -x + 4/3, z - 1/6$; (c) $1 - y, 1 + x - y, z$; (d) $-x + y, 1 - x, z$; (e) $-x + 4/3, -x + y + 2/3, -z + 7/6$. ^[a] D: donor; A: acceptor. ^[b] α : dihedral angle between the planes (°), DC: distance between the centroids of the rings (Å), α : angle (°) between mean plane of the rings. β : angle (°) between the normal to the first ring and the DC vector (°), DZ: interplanar distance (Å), DX Y: lateral displacement (Å), ^[c] p: pentagonal ring of the adeninato. p1: C14, C15, N17, C18, N19.

Table S7.- Hydrogen bonding parameters (Å, °) and π - π interactions in compound **Cu₆Cu**.¹

Cu₆Cu					
D-H...A^[a]	H...A	D...A	D-H...A		
O2-H2... O12	1.92	2.773(1)	173		
O1w-H11w...O2w ^a	2.10	2.952(1)	171		
O1w-H11w...O11 ^a	1.83	2.636(1)	156		
π - π interactions ^[b]					
Ring...Ring	α	DC	β	DZ	DX Y
p1A... p1A ^[c]	8	3.95	25.5	3.567(1)	1.70

¹Symmetry codes: (a) $-x + 1, -y, z$. ^[a] D: donor; A: acceptor. ^[b] α : dihedral angle between the planes (°), DC: distance between the centroids of the rings (Å), α : angle (°) between mean plane of the rings. β : angle (°) between the normal to the first ring and the DC vector (°), DZ: interplanar distance (Å), DX Y: lateral displacement (Å), ^[c] p: pentagonal ring of the adeninato. p1A: N17, C18, N19, C14, C15A; p2A: N21, C22, N23, C24, C25.

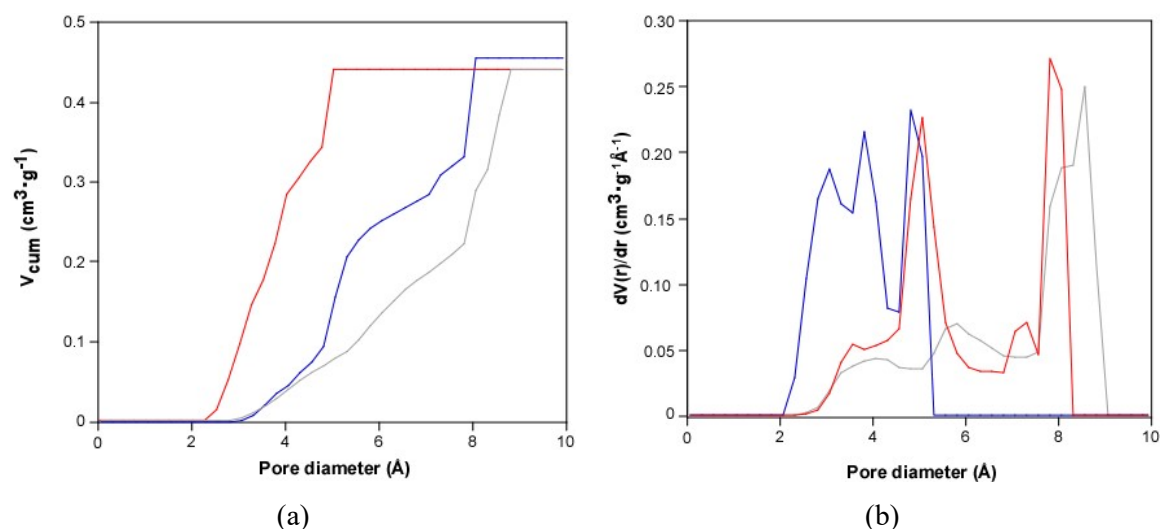
Table S8.- Hydrogen-bonding parameters (Å, °) and π - π in compound **Cu₆Co**.¹

Cu₆Co					
D-H...A ^[a]	H...A		D...A	D-H...A	
N16A-H16A...O2S ^a	1.82		2.636(4)	157	
N16A-H16A...O3w ^a	1.77		2.602(5)	162	
N16B-H16D...O3w ^a	2.45		3.286(5)	165	
π-π interactions ^[b]					
Ring...Ring	α	DC	β	DZ	DXY
p1A...p1B ^[c]	0	5.18(2)	41.6	3.01(2)	3.60

¹ Symmetry-codes: (a) $1/3 + x - y, -2/3 - y, 1/6 - z$. ^[a] D: donor; A: acceptor. ^[b] α : dihedral angle between the planes (°), DC: distance between the centroids of the rings (Å), α : angle (°) between mean plane of the rings. β : angle (°) between the normal to the first ring and the DC vector (°), DZ: interplanar distance (Å), DXY: lateral displacement (Å), ^[c] h: hexagonal ring of the adeninato and p: pentagonal ring of the adeninato ligand. p1A: C14A, C15A, N17A, C18A, N19A. p1B: C14B, C15B, N17B, C18B, N19B.

S5. Computational studies of the pore size distribution

To analyze the differences between the pore networks of Cu_6Co , Cu_6Zn and Cu_6Cu , we have computed their geometric pore size distribution (Fig. S5 and Table S9) by means of a Monte Carlo procedure implemented within a code developed by L. Sarkisov, in which the Lennard-Jones universal force field parameters are used to describe the MOF atoms while a probe, that gradually



increases its size, explores the free volume.[L. Sarkisov, *Molecular Simulation*, 2011, **37**, 1248]

Figure S5.- Pore size distribution analysis depicted as cumulative (a) and derivative (b) pore volume for compounds Cu_6Co (red), Cu_6Zn (grey) and Cu_6Cu (blue).

Table S9.- Report on the structure derived computed porosity for compounds Cu_6Co , Cu_6Zn and Cu_6Cu using a 1.2 Å probe (He).

	Porosity (%)	Void volume (cm^3/g)	Surface area (m^2/g)	Pore diameter	
				Limiting (Å)	Maximum (Å)
Cu_6Co	51.9 %	0.456	1038	4.05	8.10
Cu_6Zn	50.2 %	0.440	913	3.53	8.92
Cu_6Cu	29.4 %	0.206	116	2.85	5.09

S6. Structural flexibility of Cu_6Cu upon dehydration/hydration cycles

To analyze the structural stability of compound Cu_6Cu upon dehydration (degasification) processes, PXRD experiments were conducted over the as synthesized sample (filtered sample in Figure S6), over the same sample after activating at 30°C for 6h under high vacuum conditions, and finally after being placed in a moisture saturated environment for 24 h. It is clearly visible how the initial crystalline sample evolves into a less crystalline state in which only two quite broad peaks are clearly visible (indicative of a strong structural rearrangement). However, the flexible nature of the supramolecular architecture of this compound allows its structural recovery upon exposure to a humid atmosphere.

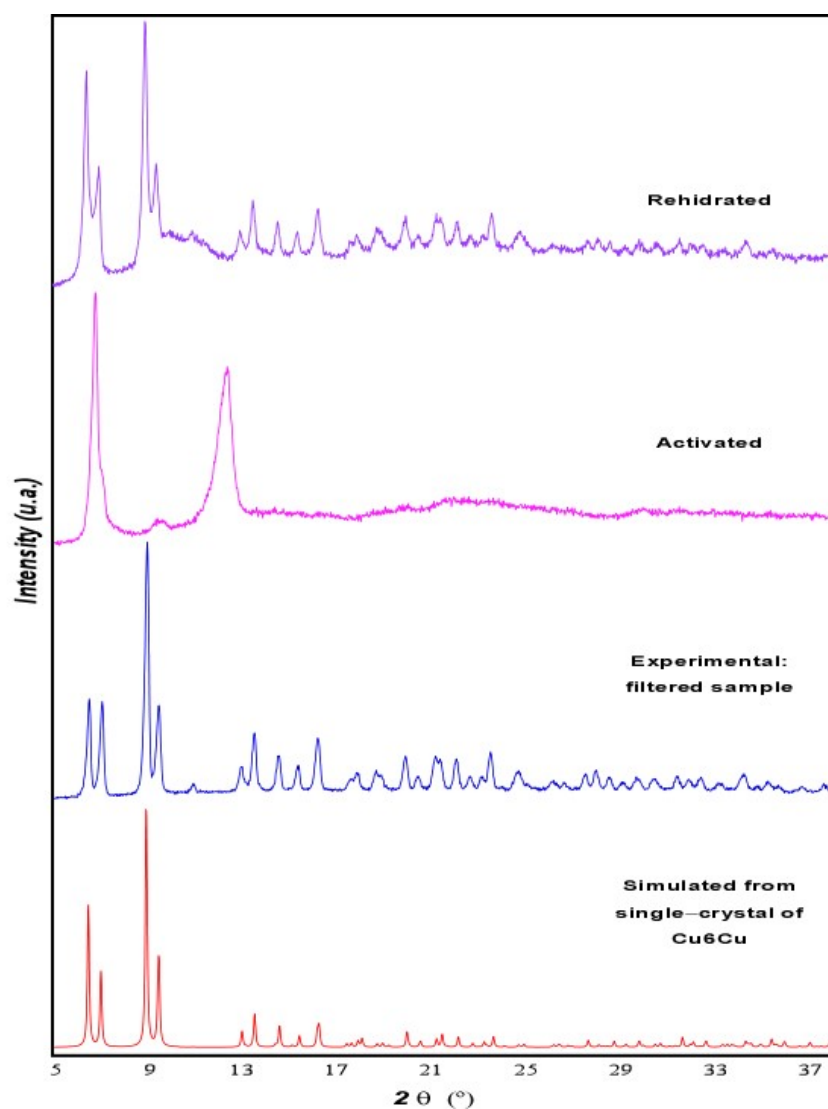


Figure S6.- PXRD data of compound Cu_6Cu after exposure to different conditions.

S7. SEM micrographs of compound Cu_6Cu

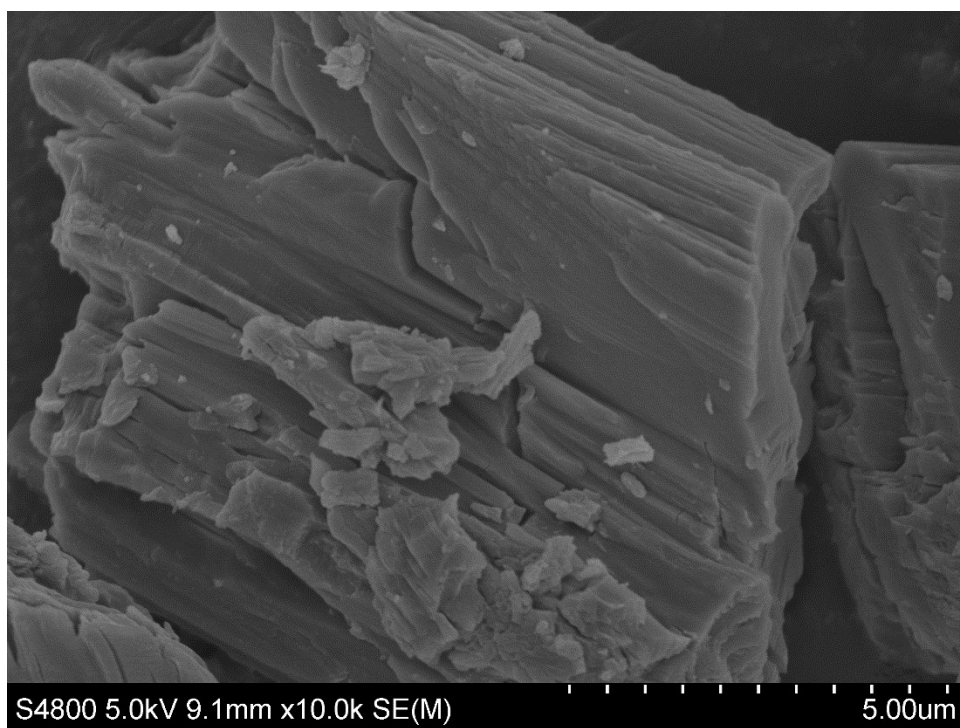
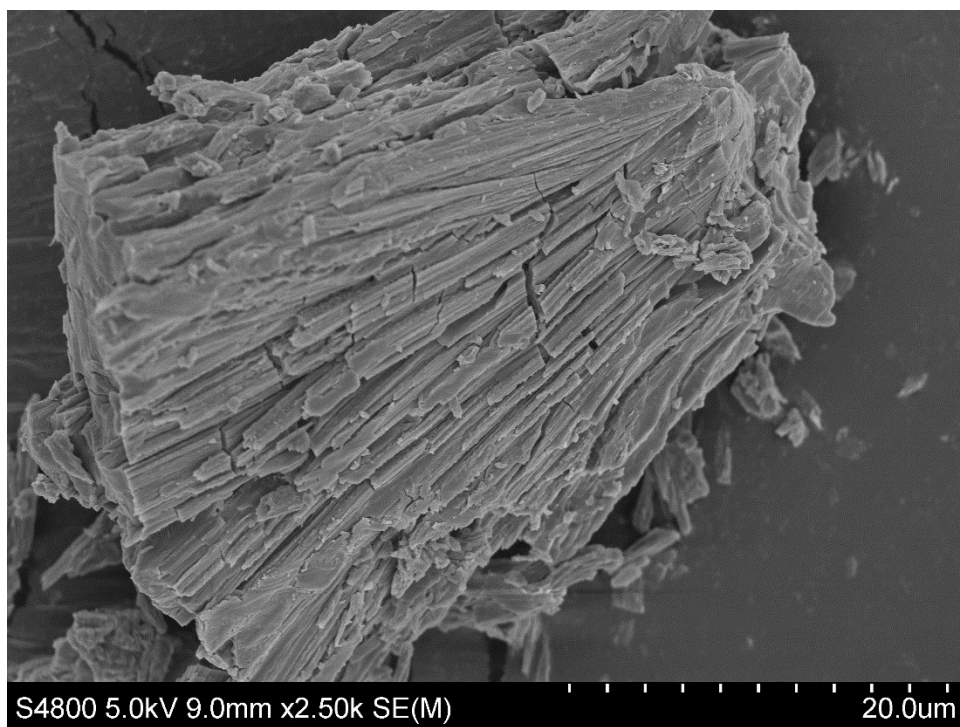
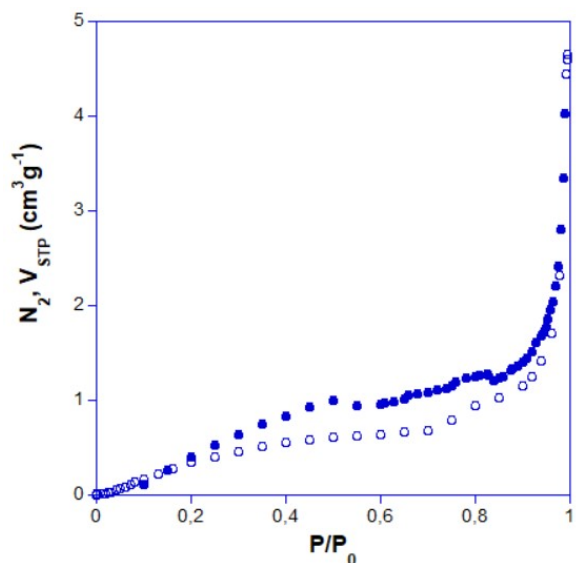


Figure S7.- SEM micrographs of compound Cu_6Cu at different magnifications.

S8. N₂ adsorption isotherms at 77 K for compound Cu₆Cu

N₂ adsorption isotherm (77 K) for compound **Cu₆Cu** was measured (Fig. S7) after outgassing the sample 6 h under vacuum at 30 °C. The results indicate a negligible adsorption ($S_{\text{BET}} = 3.5 \text{ m}^2\text{g}^{-1}$) which can be related to the structural transformation taking place during the degasification process that leads to a basically non-



porous material.

Fig. S8 N₂ adsorption isotherms at 77 K for **Cu₆Cu** (sorption branch: filled symbols; desorption branch: empty symbols).

Quantachrome® ASiQwin™- Automated Gas Sorption Data Acquisition and Reduction © 1994-2014, Quantachrome Instruments version 4.0		
Sample Desc: Heptamero de Ruben Activación 6h 30°C equil 1 minComment:Heptamero_Ruben. Activación: 6h 30 °C equil 1min		
Sample Weight: 0.103 g	Instrument: Autosorb iQ Station 1	Extended info: Available
Approx. Outgas Time: 6.2 hrs	Final Outgas Temp.: 105 °C	CellType: 6mm w/o rod
Analysis gas: Nitrogen	Non-ideality: 6.58e-05 1/Torr	Bath temp.: 77.35 K
Analysis Time: 3:05 hr:min		VoidVol Remeasure: off
Analysis Mode: Standard		Warm Zone V: 7.53081 cc
VoidVol. Mode: He Measure	Cold Zone V: 6.66711 cc	
Data Reduction Parameters		
Thermal Transpiration: onEff. mol. diameter (D): 3.54 ÅEff. cell stem diam. (d): 4.0000 mm		
Adsorbate modelNitrogen	Temperature 77.350K	Liquid Density: 0.808 g/cc
Molec. Wt.: 28.013	Cross Section: 16.200 Å²	
Relative Pressure P/Po	Volume @ STP cc/g	1 / [W((Po/P) - 1)] 1/g
1.01303e-01	0.1680	5.3674e+02
1.30893e-01	0.2218	5.4337e+02
1.60862e-01	0.2773	5.5314e+02
2.00799e-01	0.3424	5.8711e+02
BET summary		
Slope =	501.839 1/g	
Intercept =	4.806e+02 1/g	
Correlation coefficient, r =	0.953470	
C constant =	2.044	
Surface Area =	3.545 m²/g	

S9. Magnetic orbital countercomplementarity

It is well known that non-linear NCN bridges cause antiferromagnetic coupling while μ -oxo bridges are able to transmit both ferromagnetic and antiferromagnetic interactions depending on the M–O–M angle and the orientation of the metal-centered magnetic orbitals.[S. Pérez-Yáñez, O. Castillo, J. Cepeda, J. P. García-Terán, A. Luque, P. Román, Eur. J. Inorg. Chem. 2009, 3889–3899] However, the coexistence of these two types of bridges requires a more exhaustive analysis than when there is only one type. In fact, when the bridging ligands are different, the two bridges may either add or counterbalance their effects. This problem has been treated by Nishida et al.[Y. Nishida, S. Kida, J. Chem. Soc., Dalton Trans. 1986, 2633–2640] and McKee et al.,[V. McKee, M. Zvagulis, C. A. Reed, Inorg. Chem. 1985, 24, 2914–2919] and these phenomena are known as orbital complementarity and countercomplementarity, respectively. In the present case, the splitting of the molecular magnetic orbitals is reversed for each type of bridging ligand, thus leading an almost negligible energy difference between them (see qualitative MO diagram in Fig. S8). This small energy difference is responsible for the observed ferromagnetic coupling observed for the external copper(II) metal centers.

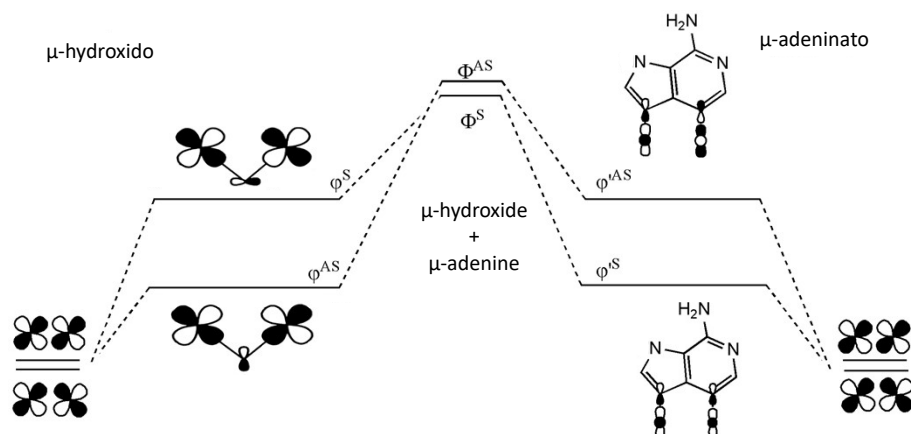


Figure S9.- Energy splitting of the $d_{x^2-y^2}$ -based magnetic orbitals leading to a ferromagnetic exchange pathway due to an orbital countercomplementarity effect.

S10. Electromagnet characterization and sustantation experiment values

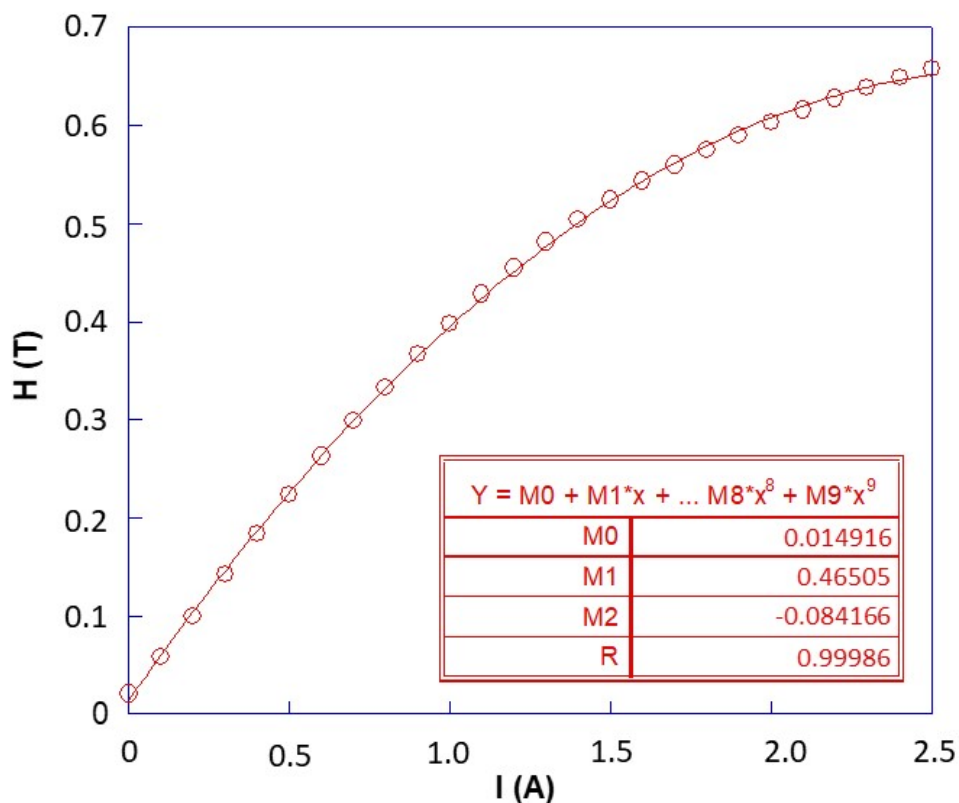


Figure S10.- Dependence of the magnetic field at the centre of the electromagnet pole with respect to electric current going through the coil of the electromagnet. The red line indicates the fitting of the data to a second order polynomial function.

Table S10.- Values of intensity going through the coil of the electromagnet necessary to maintain the particles attached to the magnetic pole (five independent measurements for each compound).

Adsorbate	Value 1	Value 2	Value 3	Value 4	Value 5	< I > (A)	σ (I)
Water	0.6437	0.6643	0.6382	0.6025	0.6356	0.6369	0.0226
CH ₃ CN	0.6566	0.6621	0.6794	0.6697	0.6718	0.6679	0.0088
DMSO	0.6697	0.6404	0.6545	0.6675	0.6564	0.6577	0.0117
THF	0.6686	0.6632	0.6653	0.662	0.6697	0.6658	0.0033
Aniline	0.8658	0.8831	0.8528	0.8929	0.8571	0.8703	0.0171
Ribose	0.7748	0.7791	0.7899	0.7856	0.7802	0.7819	0.0059
Glucose	0.7845	0.765	0.7423	0.7791	0.7748	0.7691	0.0166
Sucrose	0.7358	0.7314	0.7022	0.6816	0.7369	0.7176	0.0246
Raffinose	0.6751	0.6393	0.6296	0.5806	0.6263	0.6302	0.0338

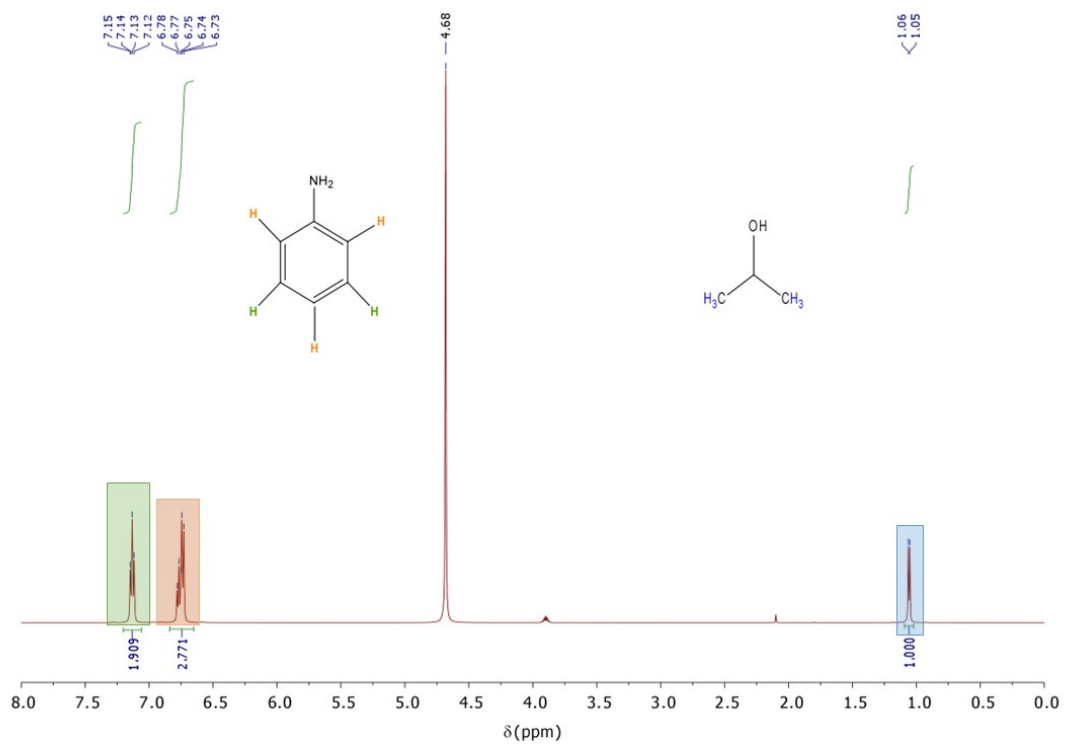
Table S11. - Intensity values transformed into magnetic field at the centre of the pole and maximum HVH data.¹H-NMR quantified sorption data.

Analyte	I (A)	σ (I)	H (T)	σ (H)	HVH	σ (HVH)	Sorption (%) ¹
Water	0.6369	0.0226	0.2764	0.0081	-0.00790	0.00048	--
CH₃CN	0.6679	0.0088	0.2880	0.0031	-0.00860	0.00019	--
DMSO	0.6577	0.0117	0.2844	0.0042	-0.00838	0.00025	--
THF	0.6658	0.0033	0.2872	0.0012	-0.00855	0.00007	--
Aniline	0.8703	0.0171	0.3559	0.0055	-0.01330	0.00042	75.2
Ribose	0.7819	0.0059	0.3271	0.0020	-0.01119	0.00014	42.9
Glucose	0.7691	0.0166	0.3228	0.0056	-0.01089	0.00039	40.2
Sucrose	0.7176	0.0246	0.3052	0.0085	-0.00971	0.00055	20.4
Raffinose	0.6302	0.0338	0.2745	0.0122	-0.00779	0.00072	--

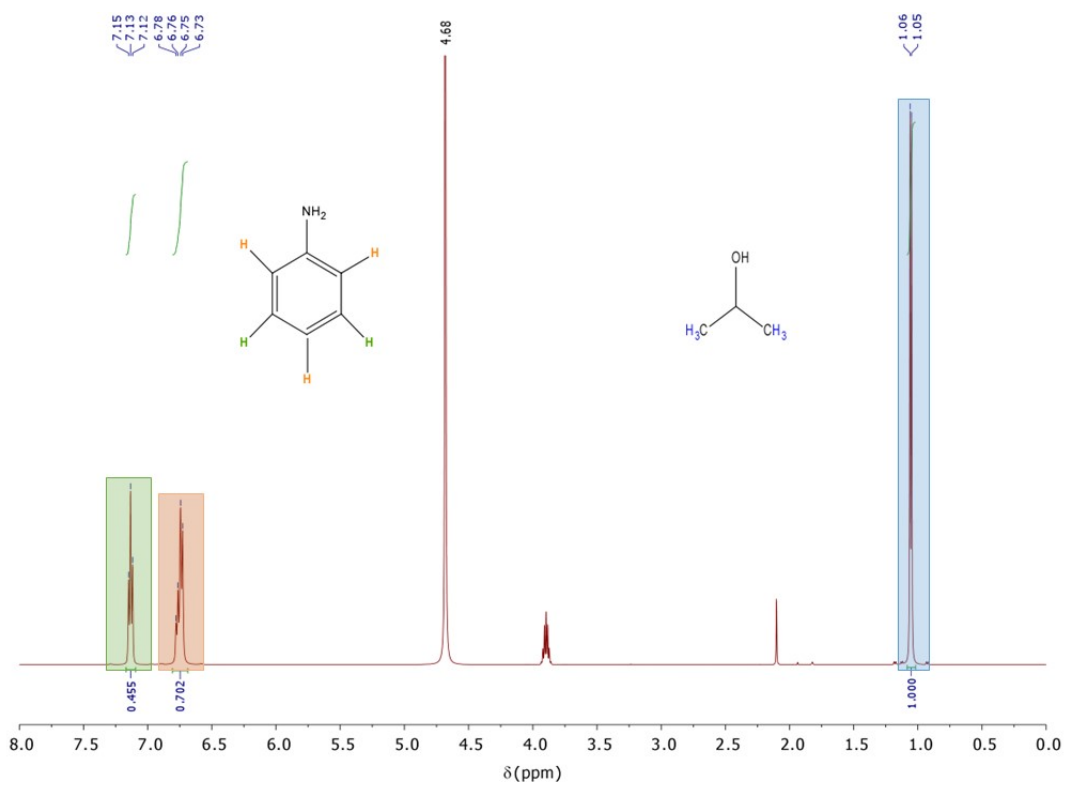
¹Sorption data quantified by ¹H-NMR (see next section)

S11. Sorption data quantification by $^1\text{H-NMR}$

$^1\text{H-NMR}$ spectra were acquired in a Bruker AVANCE 500 (one-bay; 500 MHz) at 293 K. The adsorption experiment was repeated but using D_2O : 15 mg of compound Cu_6Cu , 1.5 mL of deuterated water D_2O and 15 mg of the adsorbate of interest (aniline, ribose, glucose and sucrose) in each case. The samples were left under continuous agitation for 24h under room conditions (25°C). Later 15 μL of isopropanol were added and immediately the sample was filtered to separate the solid from the solution. The same procedure was applied for each adsorbate but without adding the porous material (Cu_6Cu) in order to set the initial adsorbate amount in the adsorption experiment. $^1\text{H-NMR}$ measurement was performed on the filtered solution and the characteristic signals of the adsorbate and the isopropanol were employed to quantify the amount of it remaining in solution and by difference with the initial value to determine the amount adsorbed within the porous material. Figures S9–S12 show the blank and after the sorption experiment solution $^1\text{H-NMR}$ spectra, indicated the signals employed for the quantification.

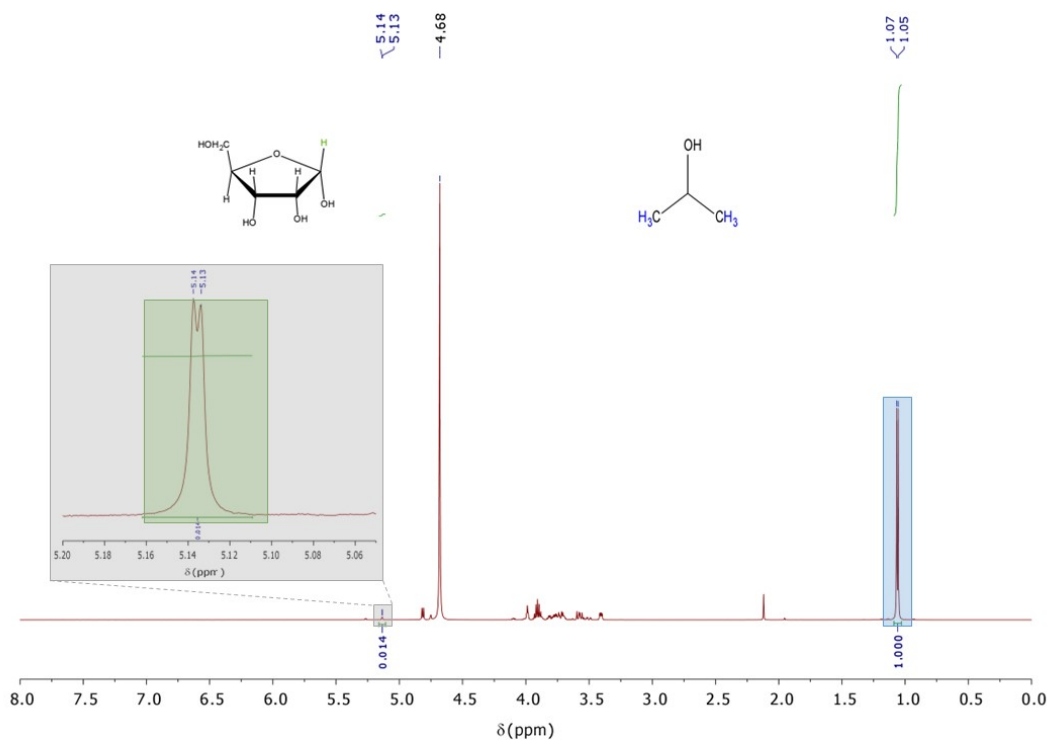


(a)

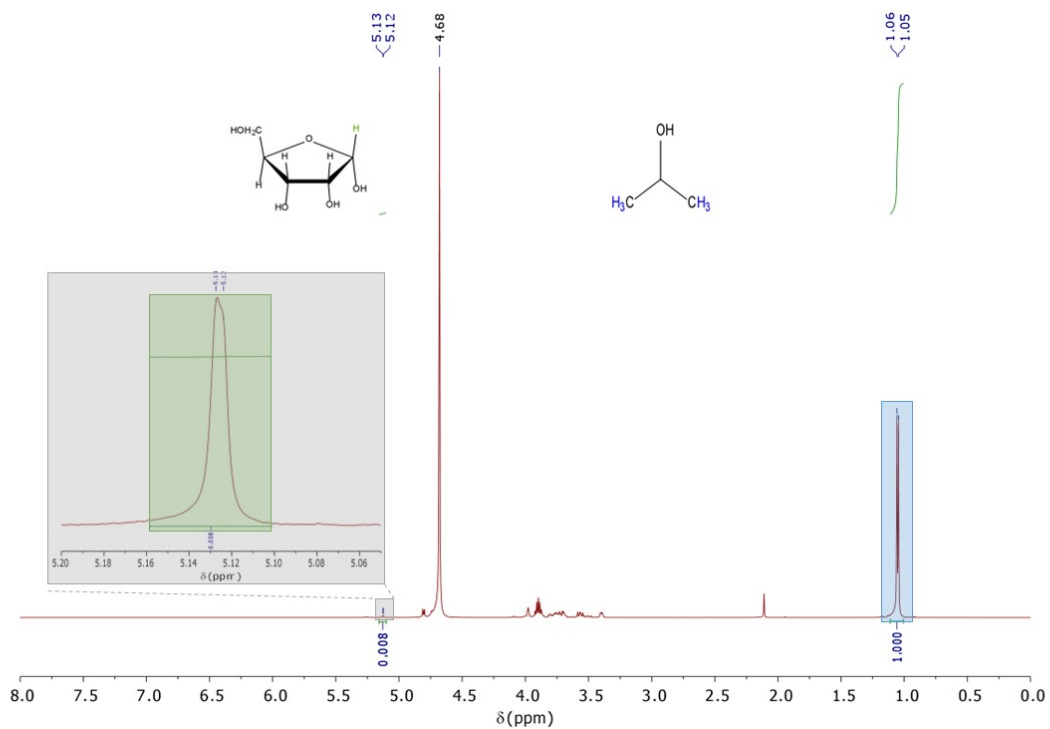


(b)

Figure S11.- $^1\text{H-NMR}$ spectra of the blank solution (a) and of the filtered sample containing the compound Cu_6Cu and aniline after 24h of continuous stirring.

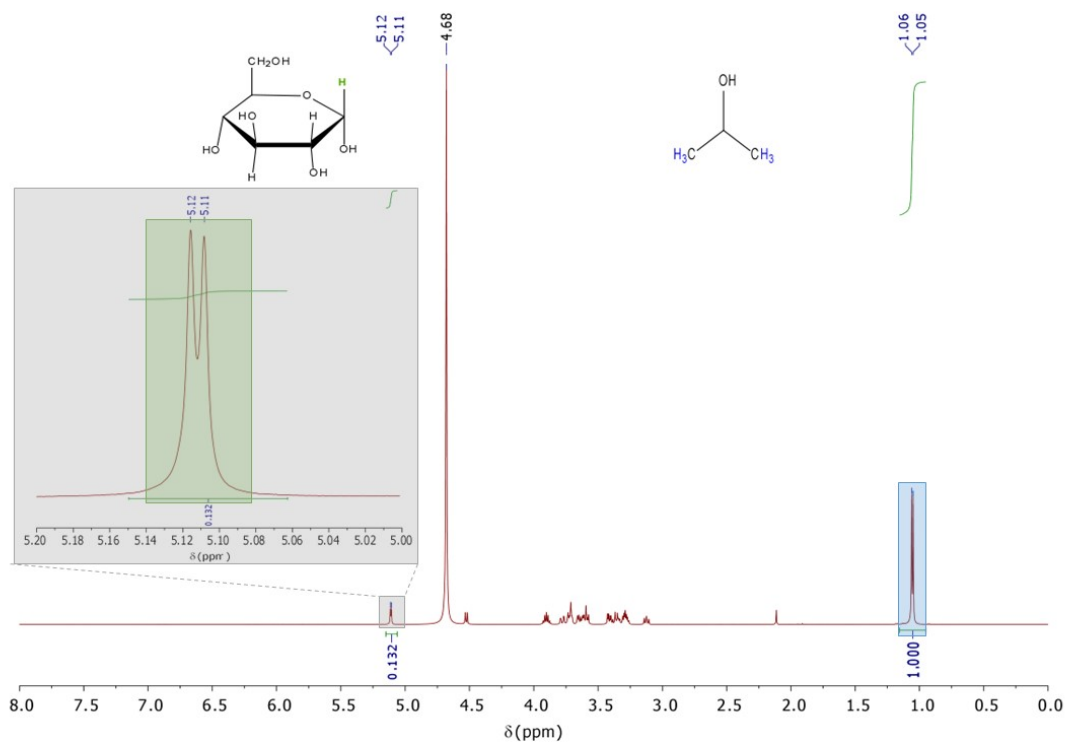


(a)

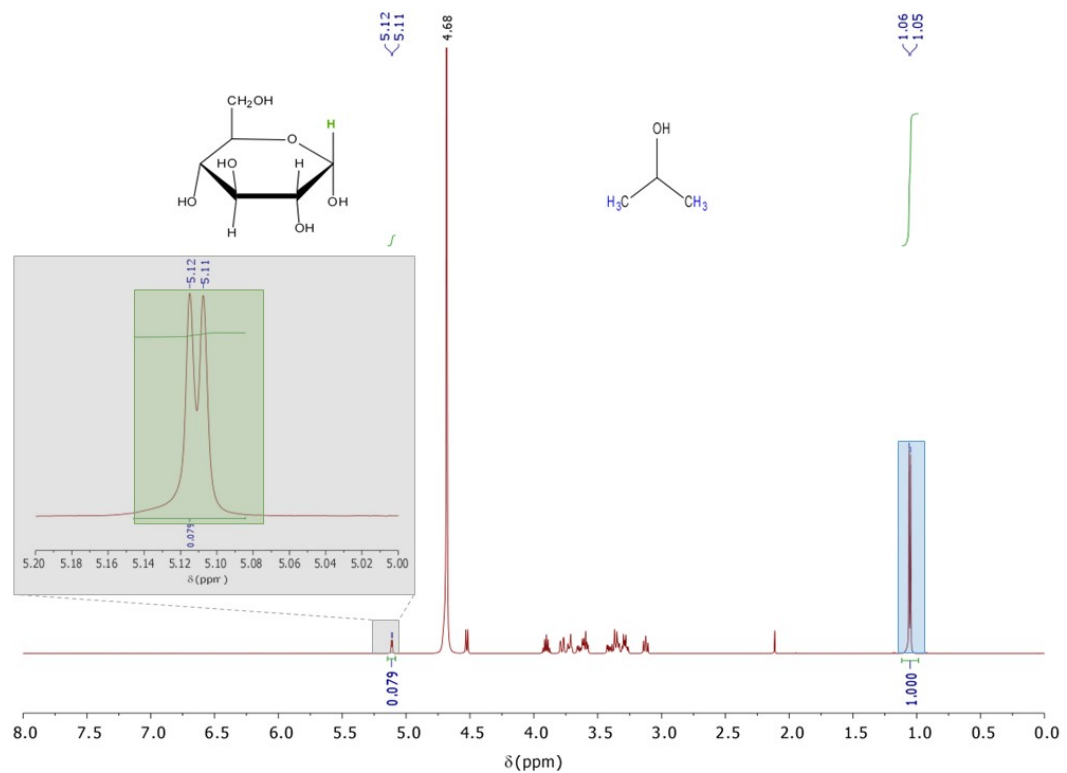


(b)

Figure S12.- ^1H -NMR spectra of the blank solution (a) and of the filtered sample containing the compound Cu_6Cu and ribose after 24h of continuous stirring.

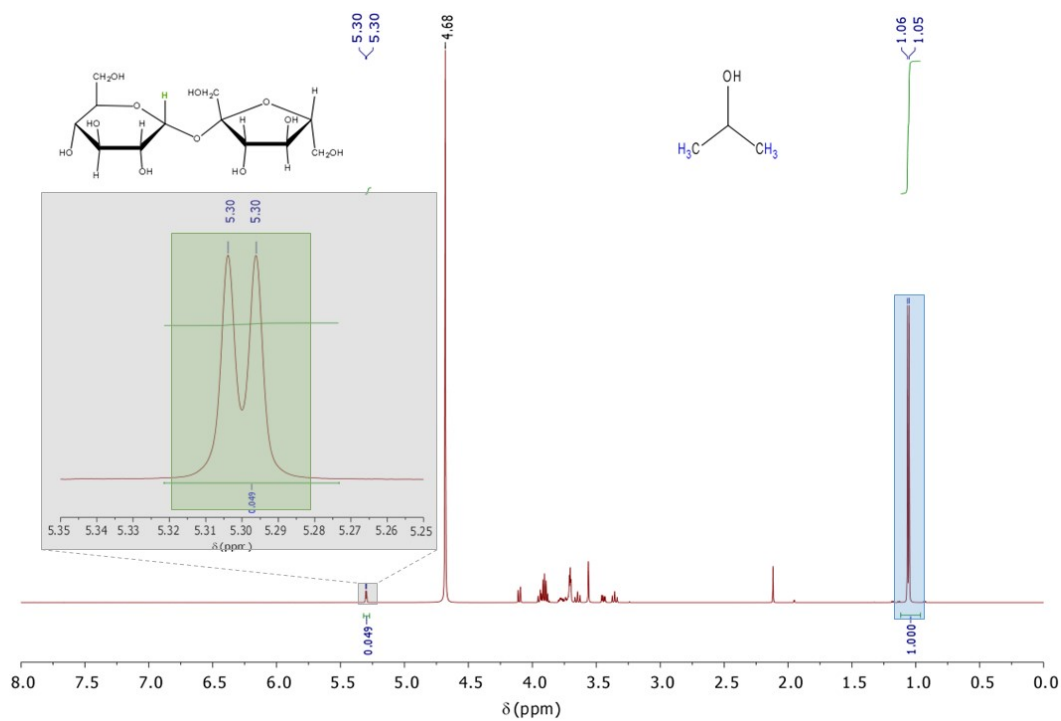


(a)

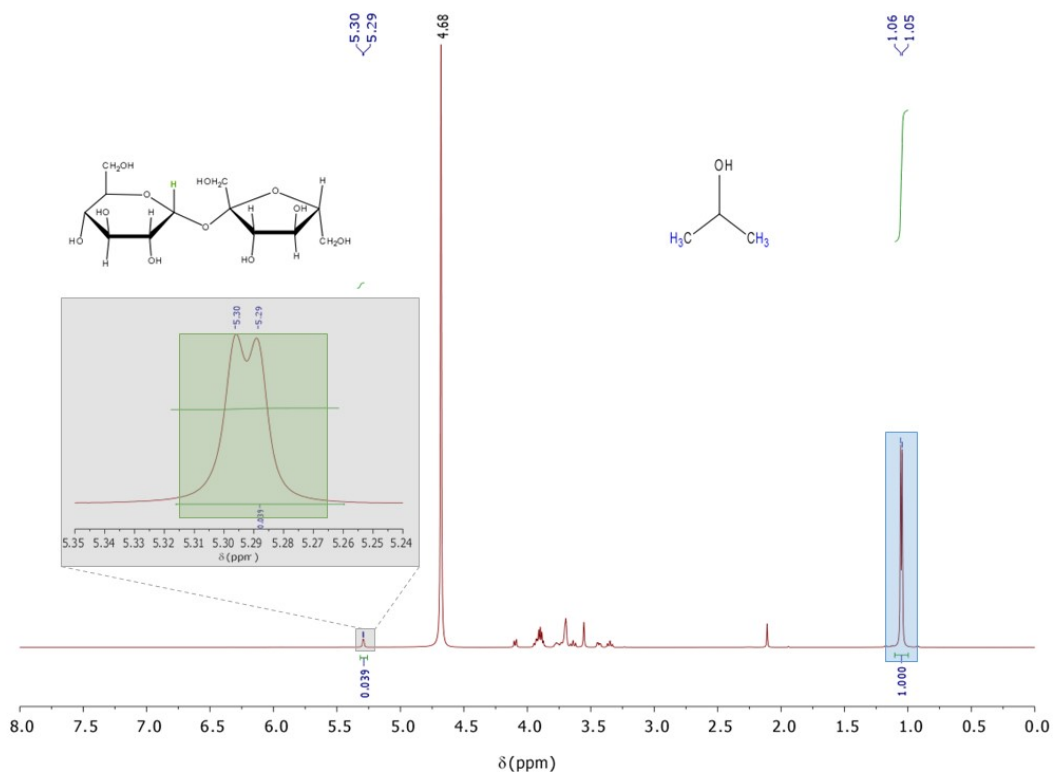


(b)

Figure S13.- $^1\text{H-NMR}$ spectra of the blank solution (a) and of the filtered sample containing the compound Cu_6Cu and glucose after 24h of continuous stirring.



(a)



(b)

Figure S14.- $^1\text{H-NMR}$ spectra of the blank solution (a) and of the filtered sample containing the compound Cu_6Cu and sucrose after 24h of continuous stirring.

S12. Elemental analysis of Cu₆Cu before and after the sorption experiments

Table S12.- CHN-Elemental analysis results.

Sample	C%	H%	N%
Cu ₆ Cu	19.2	4.2	22.4
Cu ₆ Cu·Aniline	49.8	5.0	21.5
Cu ₆ Cu·Ribose	29.4	4.0	18.0
Cu ₆ Cu·Glucose	29.1	3.9	18.5
Cu ₆ Cu·Sucrose	27.6	3.4	21.8

S13. PXRD studies of Cu_6Cu after the sorption experiments

The supramolecular crystal structure is significantly amorphized after the sorption of the different adsorbates with the remaining broad diffraction peaks displaced with respect to the pristine Cu_6Cu .

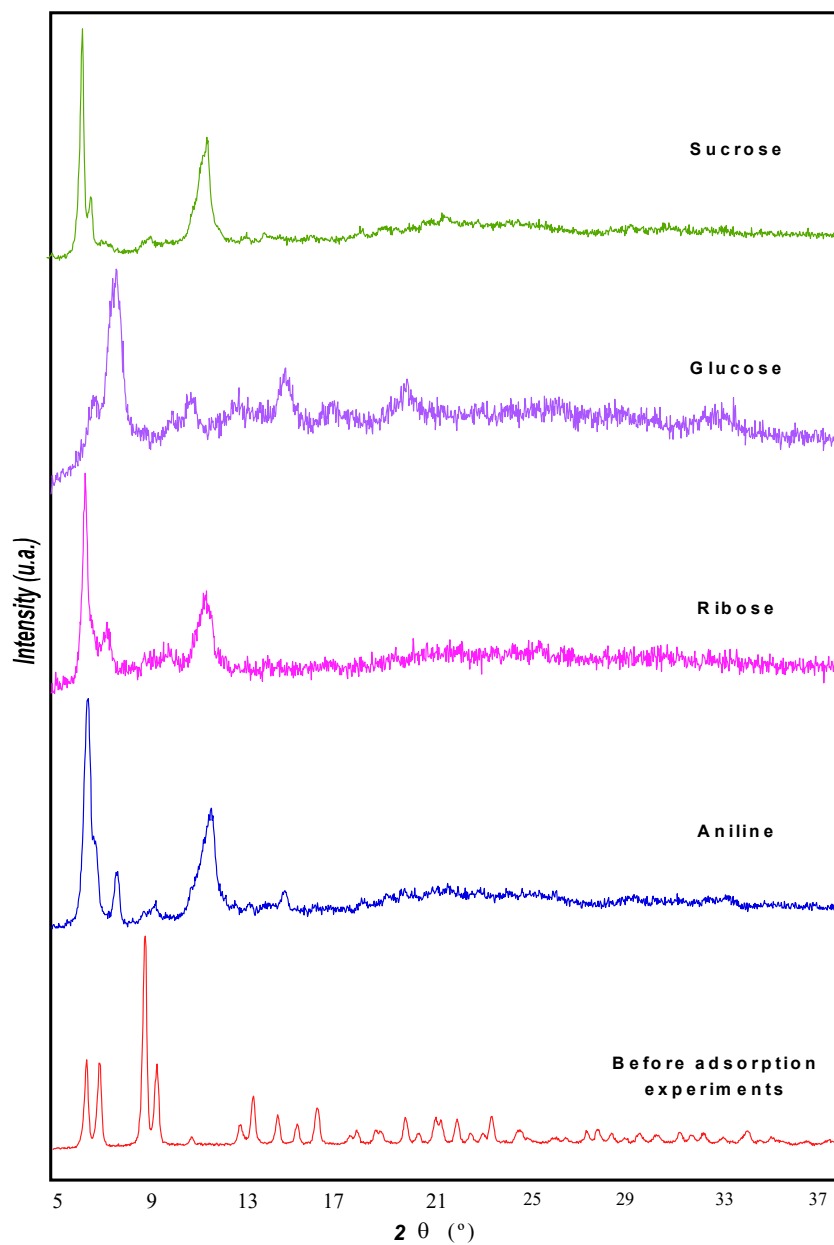


Fig. S15 PXRD pattern of Cu_6Cu after the sorption experiments.

S14. FTIR studies of Cu_6Cu after the sorption experiments

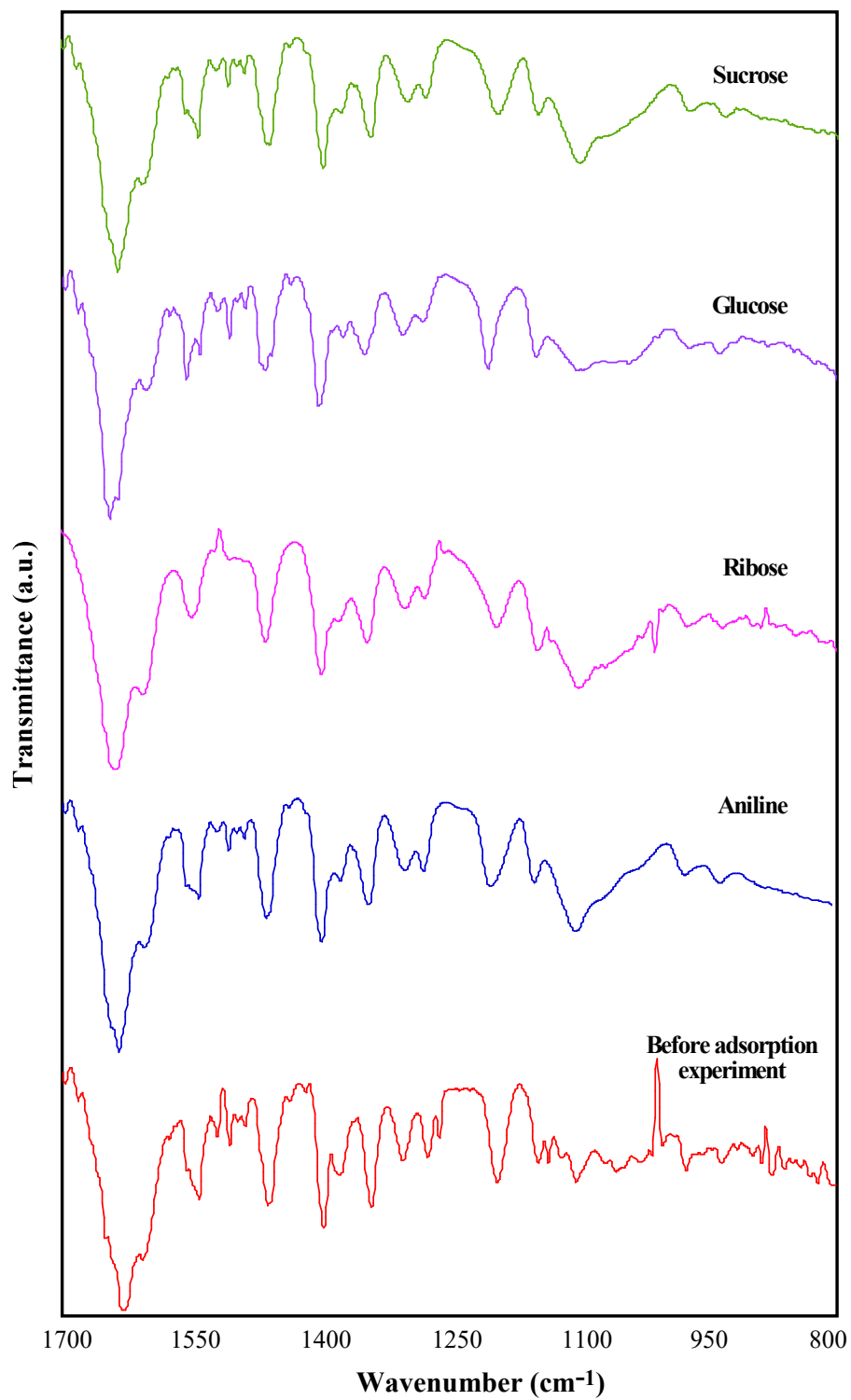


Fig. S16 FTIR spectra of Cu_6Cu before and after the sorption experiments.

S15. Comparison between the voids and adsorbate volume and shape.

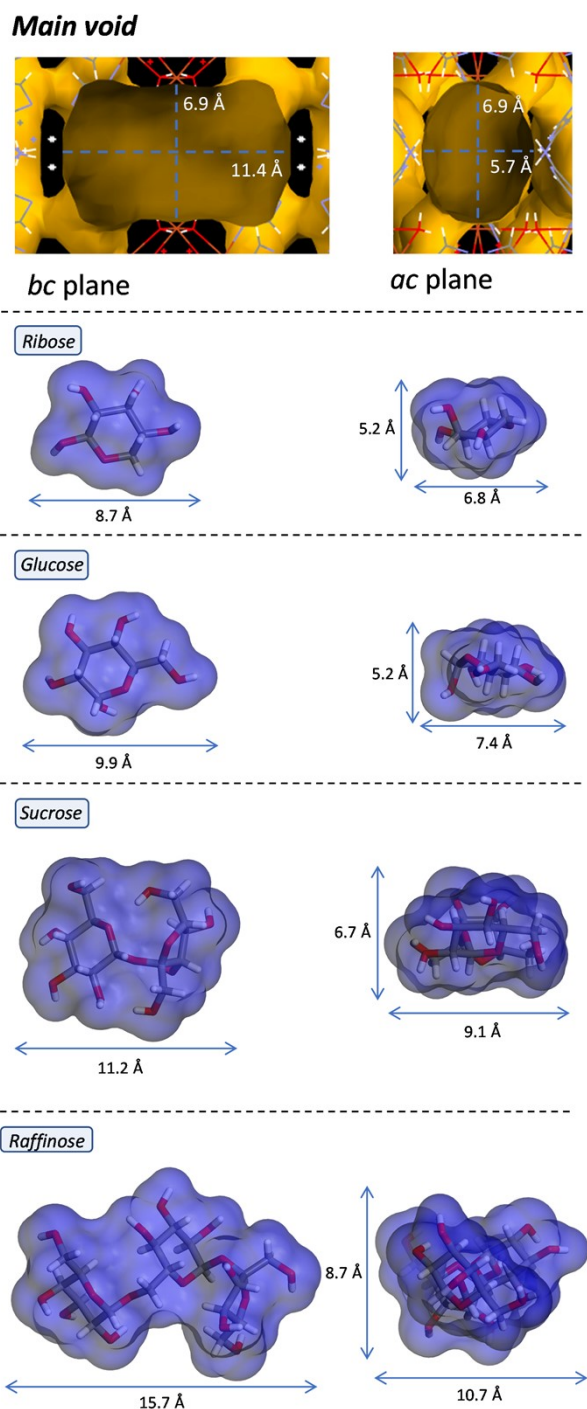


Fig. S18 Shape and dimensions of the voids present in compound Cu_6Cu and the adsorbate molecules. The same scale has been used for all the images to facilitate a direct visual comparison between them. The same probe (1.2 Å) has been employed to define the void surface (Mercury 2021.2.0) and the Connolly surface of the adsorbate molecules (Materials Studio). The conformational geometry of the saccharides has been taken from the crystal structure of these pure compounds (CCDC database).

Mercury 2021.2.0: C. F. Macrae, I. Sovago, S. J. Cottrell, P. T. A. Galek, P. McCabe, E. Pidcock, M. Platings, G. P. Shields, J. S. Stevens, M. Towler and P. A. Wood, *J. Appl. Cryst.*, 53, 226-235, 2020.

BIOVIA Materials Studio: 2017 R2 (17.2.0.1626) package.

CCDC Database: The Cambridge Structural Database. C. R. Groom, I. J. Bruno, M. P. Lightfoot and S. C. Ward, *Acta Cryst.* (2016). B72, 171-179. Refcodes: ZZZFEE01, GLUCSE02, SUCROS01, RAFINO01.

This shape and dimension comparative study helps understanding the different adsorption capacity of **Cu₆Cu** toward the saccharides. For ribose and glucose monosaccharides, their shape and dimensions fit well inside the main void of the crystal structure and as a consequence we obtain a relatively high sorption capacity. In the case of sucrose disaccharide, its dimensions are close or even slightly greater than the dimensions of the main void. However due to the flexibility of the supramolecular architecture and the conformational flexibility of sucrose it can accommodate into these voids but at the cost of a lower sorption capacity towards this adsorbate. Finally, in the case of raffinose trisaccharide, its dimensions are far above those of the main void and no sorption is observed.

It is also worth mentioning that the structural flexibility of the supramolecular building is crucial for the sorption performance of this material, as although some of these saccharides can fit into the main void their access should be hindered because of the far narrower windows that give access to it. The compound is able to overcome it because of its structural flexibility that has also been evidenced on the structural transformations taking place during the dehydration/hydration processes.